Immiscible two-phase Darcy flow model accounting for vanishing and discontinuous capillary pressures: application to the flow in fractured porous media

Konstantin Brenner, Mayya Groza, Laurent Jeannin, Roland Masson, Jeanne Pellerin

To cite this version:

Konstantin Brenner, Mayya Groza, Laurent Jeannin, Roland Masson, Jeanne Pellerin. Immiscible two-phase Darcy flow model accounting for vanishing and discontinuous capillary pressures: application to the flow in fractured porous media. 2016. hal-01338512v1

HAL Id: hal-01338512
https://hal.science/hal-01338512v1

Preprint submitted on 28 Jun 2016 (v1), last revised 15 Sep 2017 (v3)

Immiscible two-phase Darcy flow model accounting for vanishing and discontinuous capillary pressures: application to the flow in fractured porous media

Konstantin Brenner[1,2], Mayya Groza[1,2], Laurent Jeannin[3],
Roland Masson[1,2] and Jeanne Pellerin[4]

[1] Laboratoire de Mathé matiques J.A. Dieudonné, Université Nice-Sophia Antipolis, Nice
[2] Team Coffee INRIA Sophia Antipolis Méditerranée, Valbonne
[3] Weierstrass Institute, Berlin
[4] GDF SUEZ E&P, Paris

June 28, 2016

Abstract

Fully implicit time-space discretizations applied to the two-phase Darcy flow problem lead to the systems of nonlinear equations, which are traditionally solved by some variant of Newton's method. The efficiency of the resulting algorithms heavily depends on the choice of the primary unknowns since Newton's method is not invariant with respect to a nonlinear change of variable. In this regard the role of capillary pressure/saturation relation is paramount because the choice of primary unknowns is restricted by its shape. We propose an elegant mathematical framework for two-phase flow in heterogeneous porous media resulting in a family of formulations, which apply to general monotone capillary pressure/saturation relations and handle the saturation jumps at rocktype interfaces. The presented approach is applied to the hybrid dimensional model of two phase water-gas Darcy flow in fractured porous media for which the fractures are modeled as interfaces of co-dimension one. The problem is discretized using an extension of Vertex Approximate Gradient scheme. As for the phase pressure formulation, the discrete model requires only two unknowns by degree of freedom.

1 Introduction

We consider a hybrid dimensional model of two-phase gas-water Darcy flow in fractured porous media. This type of models, introduced in [1], [2] for single phase Darcy flows and in [3], [4], [5], [6] for two-phase Darcy flows, treats fractures as interfaces of co-dimension 1. We will also assume that the pressure of the phases is continuous at the interfaces between the fractures and the matrix domain, which corresponds physically to pervious fractures for which the ratio of the transversal permeability of the fracture to the width of the fracture is large compared with the ratio of the permeability of the matrix to the size of the domain. Note that it does not cover the case of fractures acting as barriers for which the pressure is discontinuous at the matrix fracture interfaces and which are considered in [7], [8], [9], [10], [11] , [12], [13] for single phase flows.

In the framework of two-phase Darcy flows in fractured porous media, highly contrasted capillary pressure curves are expected in particular between the matrix and the fractures. Hence, it is crucial to take into account in the model formulation the saturation jumps at the matrix fracture interfaces. In order to do so, as it has been stressed out in [14], the capillary pressure curves have to be extended into the monotone graphs (see e.g. Figures 2).

In several recent works [15], [6], the Vertex Approximate Gradient (VAG) discretization, employing phase pressures formulation, was applied to model two-phase Darcy flows in heterogeneous porous media. In the context of vertex-centered schemes the phase pressures formulation allows to capture the saturation jump condition at the interface between different rocktypes without introducing any additional unknowns at these interfaces. It is, however, limited to strictly increasing capillary pressure curves and lacks robustness compared to pressure-saturation formulation. In this article we extend the scheme introduced in [6] to the case of general increasing capillary pressure curves.

Let Ω be a bounded domain of $\mathbf{R}^d$, $d = 2, 3$ assumed to be polyhedral for $d = 3$ and polygonal for $d = 2$. To fix ideas the dimension will be fixed to $d = 3$ when it needs to be specified, for instance in the naming of the geometrical objects or for the space discretization in the next section. The adaptations to the case $d = 2$ are straightforward. Let $\overline{\Gamma} = \bigcup_{i\in I} \overline{\Gamma}_i$ denotes the network of fractures $\Gamma_i \subset \Omega$, $i \in J$, such that each Γ_i is a planar polygonal simply connected open domain included in some plane of $\mathbf{R}^d$ (see Figure 1).

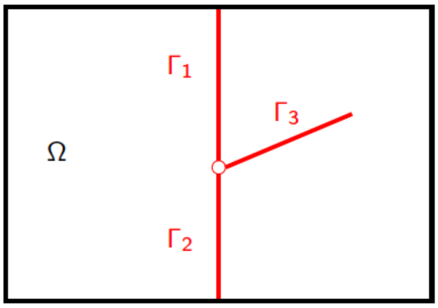

Figure 1: Example of a 2D domain Ω with 3 intersecting fractures $\Gamma_i, i = 1, 2, 3$.

In the matrix domain Ω (resp. in the fracture network Γ), we denote by $\phi_m(\mathbf{x})$ (resp. $\phi_f(\mathbf{x})$) the porosity and by $\Lambda_m(\mathbf{x})$ (resp. $\Lambda_f(\mathbf{x})$) the permeability (resp. tangential permeability) tensor. For each phase $\alpha = w, g$ (where w stands for "water" and g for "gas") we denote by $k^\alpha_{r,m}(s, \mathbf{x})$ (resp. $k^\alpha_{r,f}(s, \mathbf{x})$), the phase relative permeabilities and by $S^g_m(p, \mathbf{x})$ (resp. $S^g_f(p, \mathbf{x})$) the possibly set-valued inverses of the monotone graph extension of the capillary pressure curves. For $\alpha = w, g$, we will also denote by ρ^α the phase densities and by μ^α the phase viscosities which for the sake of clarity are assumed constant.

We denote by u^α the pressure of phase $\alpha = w, g$ and by s^g_m (resp. s^α_f) the saturation of gas phase in matrix (resp. fracture network) domain. For $i = m, f$ we define the water saturation by

$$s^w_i = 1 - s^g_i.$$

The Darcy flux of phase $\alpha = w, g$ in the matrix domain is defined by

$$\mathbf{q}^\alpha_m = -\frac{k^\alpha_{r,m}(s^\alpha_m, \mathbf{x})}{\mu^\alpha} \Lambda_m(\nabla u^\alpha - \rho^\alpha \mathbf{g}),$$

where $\mathbf{g} = g\nabla z$ stands for the gravity vector. The flow in matrix domain is described by the mass balance equation

$$\phi_m \partial_t s^\alpha_m + \mathrm{div}(\mathbf{q}^\alpha_m) = 0 \tag{1}$$

and the macroscopic capillary pressure law

$$s^g_m \in S^g_m(u^g - u^w, \mathbf{x}). \tag{2}$$

On each fracture Γ_i, $i \in I$, we denote formally by γ_i the trace operator, by ∇_{τ_i} the tangential gradient and by div_{τ_i} the tangential divergence. In addition, for all $i \in I$, we can define the two sides $\pm$ of the fracture Γ_i in $\Omega \setminus \overline{\Gamma}$ and the corresponding unit normal vectors $\mathbf{n}^\pm_i$ at Γ_i outward to the sides $\pm$. Let $\mathbf{q}^{\alpha,\pm}_m \cdot n^\pm_i$ formally denote the two normal traces of matrix fluxes at the fracture Γ_i. The Darcy flux of phase $\alpha = w, g$ in the fracture Γ_i integrated other the width of the fracture is defined by

$$\mathbf{q}^\alpha_{f,i} = -d_f \frac{k^\alpha_f(s^\alpha_f, \mathbf{x})}{\mu^\alpha} \Lambda_f(\nabla_{\tau_i} \gamma_i u^\alpha - \rho^\alpha \mathbf{g}_{\tau_i}),$$

with $\mathbf{g}_{\tau_i} = \mathbf{g} - (\mathbf{g} \cdot \mathbf{n}^+_i)\mathbf{n}^+_i$. The flow in each fracture Γ_i is described by

$$d_f \phi_f \partial_t s^\alpha_f + \mathrm{div}_{\tau_i}(\mathbf{q}^\alpha_{f,i}) - \mathbf{q}^{\alpha,+}_m \cdot \mathbf{n}^+_i - \mathbf{q}^{\alpha,-}_m \cdot \mathbf{n}^-_i = 0 \tag{3}$$

and

$$s_f^g \in S_f^g(\gamma_i u^g - \gamma_i u^w, \mathbf{x}). \tag{4}$$

The hybrid dimensional two-phase flow model looks for s_m^g, s_f^g, and $(u^\alpha)_{\alpha=g,w}$ satisfying (1)-(4). In addition to (1)-(4) we prescribe a no-flux boundary conditions at the tips of the immersed fractures, that is to say on $\partial\Gamma \setminus \partial\Omega$, and the mass conservation and pressure continuity conditions at the fracture intersections. We refer to [6] for more details on those conditions. Finally, one should provide some appropriate initial and boundary data.

Remark that for a fixed $x \in \Omega$ (resp. $x \in \Gamma$) the functions S_m^g and S_f^g are, generally speaking, set-valued, this is the case e.g. when the capillary pressure is neglected. Indeed, in such situation the gas saturation takes any value in $[0,1]$ as long as $u^g - u^w = 0$. In addition, S_m^g and S_f^g depend on space variable $\mathbf{x}$ and we will assume that $S_m^g(\cdot, \mathbf{x})$ is piecewise constant and is defined with respect to a set of so-called rocktypes. The following assumptions hold on S_m^g and S_f^g

- (A_1) Ω can be decomposed into a set of disjoint connected open polyhedral sets $(\Omega_j)_{j\in J_m}$ with $\bigcup_{j\in J_m} \overline{\Omega_j} = \overline{\Omega}$, such that $S_m^g(p, \mathbf{x}) = S_{m,j}^g(p, \mathbf{x})$ for a.e. $\mathbf{x} \in \Omega_j$ and all $p \in \mathbf{R}$. Similarly, we suppose that there exists a family of disjoint connected polygonal open sets $(\Upsilon_j)_{j\in J_f}$ such that $\bigcup_{j\in J_f} \overline{\Upsilon_j} = \overline{\Gamma}$ and such that $S_f^g(p, \mathbf{x}) = S_{f,j}^g(p)$ for a.e. $\mathbf{x} \in \Upsilon_j$ and all $p \in \mathbf{R}$.
- (A_2) $\left(S_{m,j}^g\right)_{j\in J_m}$ and $\left(S_{f,j}^g\right)_{j\in J_f}$ are maximal monotone graphs with domain $\mathbf{R}$ and satisfying $S_{i,j}^g(p) \subset [0,1]$ for all $p \in \mathbf{R}$ and $i = m, f$, $j \in J_i$.

The matrix and fracture relative permeabilities are piecewise constant w.r.t. $\mathbf{x}$ on the same partitions of the matrix and fracture network domains as the capillary pressure curves. In the following, we will denote the mobilities (ratio of the phase relative permeability to the phase viscosity) by $k_{m,j}^\alpha(s)$ in the matrix for each rocktype $j \in J_m$ and by $k_{f,j}^\alpha(s)$ in the fracture network for each rocktype $j \in J_f$.

In order to illustrate the difficulty of dealing with both heterogeneous and multi-valued saturation curves S_m^g and S_f^g, let us admit for the moment that S_m^g are S_f^g do not depend on $\mathbf{x}$ and that $S_m^g(p)$, $S_f^g(p)$ are single-valued continuous increasing functions satisfying for $i = m, f$

$$S_i^g(p \le p_{ent,i}) = 0 \text{ and } \lim_{p\to+\infty} S_i^g(p) = 1$$

with $p_{ent,i} \in \mathbf{R}$, $i = m, f$ been an entry pressure. The figure 2a exhibits a typical form of multi-valued capillary pressure curves corresponding to $S_m^g(p)$ are $S_f^g(p)$.

When the system (1) - (4) is solved numerically it is desirable to reduce the number of unknown by eliminating the algebraic equations (2) and (4), in particular one may expect to have as much as two unknowns by degree of freedom. Note that as long as the functions S_i^g, $i = m, f$, are single valued (which is the case when the capillary pressure graphs do not have "horizontal" parts) it is possible to express s_m^g and s_f^g in terms of u^g and u^w. In other words (u^w, u^g) is an admissible couple of primary unknowns. The other admissible couple is (u^w, s_f^g) since u^g and s_m^g can be expressed as

$$u^g = u^w + (S_f^g)^{-1}(s_f^g) \text{ and } s_m^g = S_m^g \circ (S_f^g)^{-1}(s_f^g).$$

In contrast, unless $p_{ent,m}$ is less or equal to $p_{ent,f}$, it is not possible to describe any possible values of u^g and s_f^g at the matrix fracture interface using the pair (u^g, s_m^g). However this formulation still can be applied "away" from Γ.

Let us remark that both (u^w, u^g) and (u^w, s_f^g) formulations lead, after a space-time discretization of (1) and (3), to the equivalent systems of nonlinear algebraic equations. Nevertheless, in practice, the performance of numerical algorithm would heavily depend on the choice of primary variables. In particular it is well known that the use of the formulation based on u^g and u^w has to be avoided when modeling imbibition in very dry soil. This is explained by the the fact that applying Newton-Raphson method (or some other linearization scheme) for solving nonlinear problems resulting from both formulation brakes the equivalence.

Next, let's assume that the capillary pressure is neglected in fracture network domain (see Figure 2b). In that case both S_f^g and its inverse are set-valued, which in particular implies that neither (u^w, s_f^g) nor (u^w, u^g) can be used as a pair of primary variables for the whole range of values of saturation and capillary pressure. Instead one may switch, as capillary pressure grows, from (u^w, s_f^g) to (u^w, u^g), and even possibly from (u^w, u^g) to (u^w, s_m^g) for $u^g - u^w \ge p_{ent,m}$. Note that if the capillary pressure in fracture domain is very small, but not strictly zero one can not expect the numerical scheme based on (u^w, s_f^g) formulation to be computationally efficient.

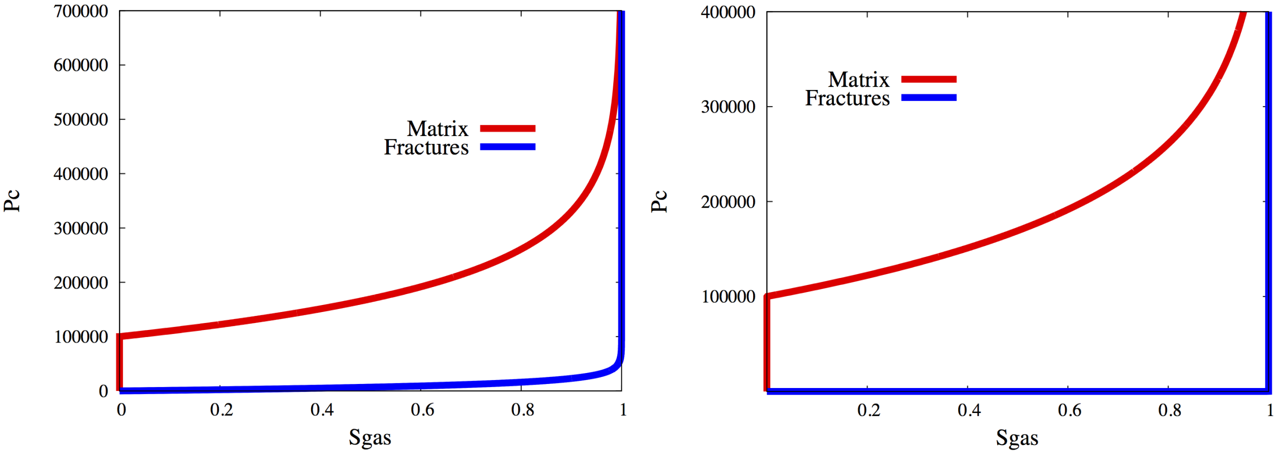

(a) S^g_m and S^g_f are single-valued (b) S^g_m is single-valued, S^g_f is set-valued

Figure 2: Typical form of capillary pressure curves in matrix and fracture domains.

Finally, let us remark that there is no reason to restrict the choice of primary variables to the set of natural variables, that is to say, to u^w, u^g, s^g_m and s^g_f. Consider continuous functions

$$\mathcal{P} \text{ and } (\mathcal{S}^g_i)_{i=m,f} \tag{5}$$

defined on an open convex set $\mathcal{I} \subset \mathbf{R}$ such that $\mathcal{P}(\mathcal{I}) = \mathbf{R}$ and such that for $\tau \in \mathcal{I}$

$$\mathcal{S}^g_i(\tau) \in S^g_i(\mathcal{P}(\tau)) \text{ for all } i = m, f. \tag{6}$$

Then the couple (u^w, τ) is an admissible couple of primary unknowns with

$$u^g = u^w + \mathcal{P}(\tau) \text{ and } s^g_i = \mathcal{S}^g_i(\tau),\ i = m, f.$$

The map $\tau \mapsto (\mathcal{P}(\tau), \mathcal{S}^g_i(\tau))$, $i = m, f$, can be seen as the parametrization of curve S^g_i. The parametrization (5) is not uniquely defined by (6) even under some additional regularity assumptions (see Proposition 3.1) and hence one can try to choose the functions $\mathcal{P}(\tau)$ and $\mathcal{S}^g_i(\tau)$, $i = m, f$, in order to improve the convergence of the nonlinear solver.

The remaining of this article is organized as follows. In the next section we briefly recall the VAG scheme introduced in [6] using u^g and u^w as primary unknowns. Then we detail the parametrization approach presented above and provide the extension of the VAG discretization accounting for general monotone capillary pressure graphs related to multiple rocktypes, and finally we present numerical experiments, which aims to compare classical pressure-saturation formulations with more advanced parametrizations using ideas presented above.

2 Vertex Approximate Gradient (VAG) Discretization

In this section, assuming that $S^g_m(\cdot, \mathbf{x})$ and $S^g_f(\cdot, \mathbf{x})$ are single valued, we will recall the construction of the numerical scheme presented in [6]. More precisely, in addition to (A_2) the following assumption holds

(A_{2a}) $\left(S^g_{m,j}\right)_{j \in J_m}$ and $\left(S^g_{f,j}\right)_{j \in J_f}$ are non decreasing continuous functions from $\mathbf{R}$ to $[0, 1]$.

The VAG discretization of hybrid dimensional two-phase Darcy flows introduced in [6] considers a generalised polyhedral meshes of Ω in the spirit of [16]. Let $\mathcal{M}$ be the set of cells that are disjoint open polyhedral subsets of Ω such that $\bigcup_{K \in \mathcal{M}} \overline{K} = \overline{\Omega}$, for all $K \in \mathcal{M}$, $\mathbf{x}_K$ denotes the so-called "centre" of the cell K under the assumption that K is star-shaped with respect to $\mathbf{x}_K$. We then denote by $\mathcal{F}_K$ the set of interfaces of non zero $d-1$ dimensional measure among the interior faces $\overline{K} \cap \overline{L}$, $L \in \mathcal{M}$, and the boundary interface $\overline{K} \cap \partial\Omega$, which possibly splits in several boundary faces. Let us denote by

$$\mathcal{F} = \bigcup_{K \in \mathcal{M}} \mathcal{F}_K$$

the set of all faces of the mesh. Remark that the faces are not assumed to be planar, hence the term "generalised polyhedral mesh". For $\sigma \in \mathcal{F}$, let $\mathcal{E}_\sigma$ be the set of interfaces of non zero $d-2$ dimensional measure among the interfaces $\overline{\sigma} \cap \overline{\sigma}'$, $\sigma' \in \mathcal{F}$. Then, we denote by

$$\mathcal{E} = \bigcup_{\sigma \in \mathcal{F}} \mathcal{E}_\sigma$$

the set of all edges of the mesh. Let $\mathcal{V}_\sigma = \bigcup_{e,e' \in \mathcal{E}_\sigma, e \neq e'} \left(e \cap e'\right)$ be the set of vertices of σ. For each $K \in \mathcal{M}$ we define $\mathcal{V}_K = \bigcup_{\sigma \in \mathcal{F}_K} \mathcal{V}_\sigma$, and we also denote by

$$\mathcal{V} = \bigcup_{K \in \mathcal{M}} \mathcal{V}_K$$

the set of all vertices of the mesh. It is then assumed that for each face $\sigma \in \mathcal{F}$, there exists a so-called "centre" of the face $\mathbf{x}_\sigma \in \sigma \setminus \bigcup_{e \in \mathcal{E}_\sigma} e$ such that $\mathbf{x}_\sigma = \sum_{\mathbf{s} \in \mathcal{V}_\sigma} \beta_{\sigma,\mathbf{s}}\, \mathbf{x}_\mathbf{s}$, with $\sum_{\mathbf{s} \in \mathcal{V}_\sigma} \beta_{\sigma,\mathbf{s}} = 1$, and $\beta_{\sigma,\mathbf{s}} \geq 0$ for all $\mathbf{s} \in \mathcal{V}_\sigma$; moreover the face σ is assumed to be defined by the union of the triangles $T_{\sigma,e}$ defined by the face centre $\mathbf{x}_\sigma$ and each edge $e \in \mathcal{E}_\sigma$. The mesh is also supposed to be conforming w.r.t. the fracture network Γ in the sense that for all $i \in I$ there exist the subsets $\mathcal{F}_{\Gamma_i}$of $\mathcal{F}$ such that $\overline{\Gamma}_i = \bigcup_{\sigma \in \mathcal{F}_{\Gamma_i}} \overline{\sigma}$. We will denote by $\mathcal{F}_\Gamma$ the set of fracture faces $\bigcup_{i \in I} \mathcal{F}_{\Gamma_i}$. This geometrical discretization of Ω and Γ is denoted in the following by $\mathcal{D}$.

The space discretization is assumed to be compatible with the sets $(\Omega_j)_{j \in J_m}$ and $(\Upsilon_j)_{j \in J_f}$, that is to say, for all $K \in \mathcal{M}$ there exists $j_K \in J_m$ such that $K \subset \Omega_{j_K}$ and for all $\sigma \in \mathcal{F}_\Gamma$ there exists $j_\sigma \in J_f$ such that $\sigma \subset \Upsilon_{j_\sigma}$. In other words, j_K is the rocktype of cell K and j_σ is the rocktype of the fracture face σ.

The VAG discretization has been introduced in [16] for diffusive problems on heterogeneous anisotropic media. Its extension to the hybrid dimensional Darcy flow model is proposed in [6] based upon the following vector space of degrees of freedom:

$$X_\mathcal{D} = \{v_K, v_\mathbf{s}, v_\sigma \in \mathbf{R}, K \in \mathcal{M}, \mathbf{s} \in \mathcal{V}, \sigma \in \mathcal{F}_\Gamma\},$$

and its subspace with homogeneous Dirichlet boundary conditions on $\partial\Omega$:

$$X^0_\mathcal{D} = \{v \in X_\mathcal{D} \,|\, v_\mathbf{s} = 0 \text{ for } \mathbf{s} \in \mathcal{V}_{ext}\},$$

where $\mathcal{V}_{ext} = \mathcal{V} \cap \partial\Omega$ denotes the set of boundary vertices, and $\mathcal{V}_{int} = \mathcal{V} \setminus \partial\Omega$ denotes the set of interior vertices. The degrees of freedom are exhibited in Figure 3 for a given cell K with one fracture face σ in bold.

The VAG scheme is a control volume scheme in the sense that it results, for each interior degree of freedom and each phase, in a mass balance equation. The two main ingredients are therefore the conservative fluxes and the control volumes. The VAG matrix and fracture fluxes are exhibited in Figure 3. For $u \in X_\mathcal{D}$, the matrix fluxes $F_{K,\nu}(u)$ connect the cell $K \in \mathcal{M}$ to the degrees of freedom located at the boundary of K, namely $\nu \in \Xi_K = \mathcal{V}_K \cup (\mathcal{F}_K \cap \mathcal{F}_\Gamma)$. The fracture fluxes $F_{\sigma,\mathbf{s}}(u)$ connect each fracture face $\sigma \in \mathcal{F}_\Gamma$ to its nodes $\mathbf{s} \in \mathcal{V}_\sigma$. Note also that the expression of the matrix (resp. the fracture) fluxes is local to the cell (resp. fracture face) and let us refer to [6] for a more detailed presentation.

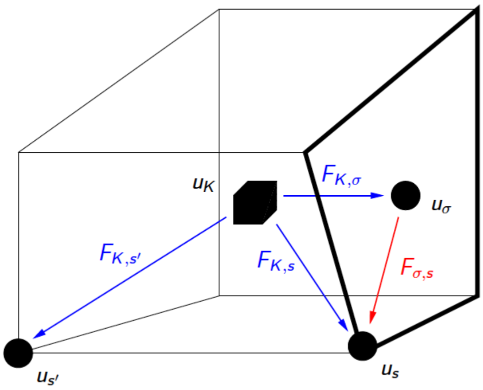

Figure 3: For a cell K and a fracture face σ (in bold), examples of VAG degrees of freedom u_K, $u_\mathbf{s}$, u_σ, $u_{\mathbf{s}'}$ and VAG fluxes $F_{K,\sigma}$, $F_{K,\mathbf{s}}$, $F_{K,\mathbf{s}'}$, $F_{\sigma,\mathbf{s}}$.

The construction of the control volumes at each degree of freedom is based on partitionings of the cells and of the fracture faces. These partitions are respectively denoted, for all $K \in \mathcal{M}$, by

$$\overline{K} = \overline{\omega}_K \bigcup \left(\bigcup_{\mathbf{s} \in \mathcal{V}_K \cap \mathcal{V}_{int}} \overline{\omega}_{K,\mathbf{s}} \right) \bigcup \left(\bigcup_{\sigma \in \mathcal{F}_K \cap \mathcal{F}_\Gamma} \overline{\omega}_{K,\sigma} \right),$$

and, for all $\sigma \in \mathcal{F}_\Gamma$, by

$$\overline{\sigma} = \overline{\Sigma}_\sigma \bigcup \left(\bigcup_{\mathbf{s} \in \mathcal{V}_\sigma \cap \mathcal{V}_{int}} \overline{\Sigma}_{\sigma,\mathbf{s}} \right).$$

It is important to notice that in the usual case of cellwise constant rocktypes in the matrix and facewise constant rocktypes in the fracture network, the implementation of the scheme does not require to build explicitly the geometry ofthese partitions. In that case, it is sufficient to define the matrix volume fractions

$$\alpha_{K,\mathbf{s}} = \frac{\int_{\omega_{K,\mathbf{s}}} d\mathbf{x}}{\int_K d\mathbf{x}}, \mathbf{s} \in \mathcal{V}_K \cap \mathcal{V}_{int}, K \in \mathcal{M},\ \alpha_{K,\sigma} = \frac{\int_{\omega_{K,\sigma}} d\mathbf{x}}{\int_K d\mathbf{x}}, \sigma \in \mathcal{F}_K \cap \mathcal{F}_\Gamma, K \in \mathcal{M},$$

constrained to satisfy $\alpha_{K,\mathbf{s}} \geq 0$, $\alpha_{K,\sigma} \geq 0$, and $\sum_{\mathbf{s} \in \mathcal{V}_K \cap \mathcal{V}_{int}} \alpha_{K,\mathbf{s}} + \sum_{\sigma \in \mathcal{F}_K \cap \mathcal{F}_\Gamma} \alpha_{K,\sigma} \leq 1$, as well as the fracture volume fractions

$$\alpha_{\sigma,\mathbf{s}} = \frac{\int_{\Sigma_{\sigma,\mathbf{s}}} d_f(\mathbf{x}) d\tau(\mathbf{x})}{\int_\sigma d_f(\mathbf{x}) d\tau(\mathbf{x})}, \mathbf{s} \in \mathcal{V}_\sigma \cap \mathcal{V}_{int}, \sigma \in \mathcal{F}_\Gamma,$$

constrained to satisfy $\alpha_{\sigma,\mathbf{s}} \geq 0$, and $\sum_{\mathbf{s} \in \mathcal{V}_\sigma \cap \mathcal{V}_{int}} \alpha_{\sigma,\mathbf{s}} \leq 1$, where we denote by $d\tau(\mathbf{x})$ the $d-1$ dimensional Lebesgue measure on Γ. Let us also set

$$\phi_K = (1 - \sum_{\nu \in \Xi_K \cap \mathcal{V}_{int}} \alpha_{K,\nu}) \int_K \phi_m(\mathbf{x}) d\mathbf{x}$$

and

$$\phi_\sigma = (1 - \sum_{\mathbf{s} \in \mathcal{V}_\sigma \cap \mathcal{V}_{int}} \alpha_{\sigma,\mathbf{s}}) \int_\sigma \phi_f(\mathbf{x}) d_f(\mathbf{x}) d\tau(\mathbf{x}),$$

as well as $\phi_{K,\nu} = \alpha_{K,\nu} \int_K \phi_m(\mathbf{x}) d\mathbf{x}$ and $\phi_{\sigma,s} = \alpha_{\sigma,\mathbf{s}} \int_\sigma \phi_f(\mathbf{x}) d_f(\mathbf{x}) d\tau(\mathbf{x})$, which correspond to the porous volume distributed to the degrees of freedom.

As it has been shown in [6], the flexibility in the choice of $\alpha_{K,s}$ and $\alpha_{\sigma,s}$ is a crucial asset, compared with usual CVFE approaches and allows to significantly improve the accuracy of the scheme when the permeability field is highly heterogeneous. As exhibited in Figure 4, as opposed with usual CVFE approaches, this flexibility allows to define the control volumes in the fractures with no contribution from the matrix in order to avoid to enlarge artificially the flow path in the fractures.

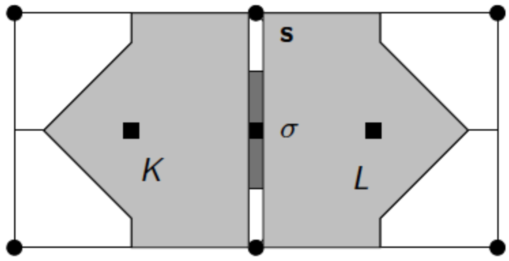

Figure 4: Example of control volumes at cells, fracture face, and nodes, in the case of two cells K and L splitted by one fracture face σ (the width of the fracture has been enlarged in this figure).

For $N \in \mathbf{N}^*$, let us consider the time discretization $t^0 = 0 < t^1 < \cdots < t^{n-1} < t^n \cdots < t^N = T$ of the time interval $[0, T]$. We denote the time steps by $\Delta t^n = t^n - t^{n-1}$ for all $n = 1, \cdots, N$.

Considering homogeneous Dirichlet boundary conditions for convenience, the VAG discretization introduced in [6] of the hybrid dimensional two phase Darcy flow model (1) - (4) looks for $u^{g,n}, u^{w,n} \in X^0_{\mathcal{D}}$, $n = 1, \cdots, N$, such that one has for all $v^\alpha \in X^0_{\mathcal{D}}$ and for $\alpha = g, w$:

$$\left\{\begin{array}{l}
\displaystyle\sum_{K\in\mathcal{M}} \left(\frac{\phi_K}{\Delta t^n}(S_K^{\alpha,n} - S_K^{\alpha,n-1}) + \sum_{\nu\in\Xi_K} k^\alpha_{m,j_K}(S^{\alpha,n}_{K,\nu,up}) F^\alpha_{K,\nu}(u^{\alpha,n}) \right) v^\alpha_K \\
\displaystyle + \sum_{K\in\mathcal{M}} \sum_{\nu\in\Xi_K\setminus\mathcal{V}_{ext}} \left(\frac{\phi_{K,\nu}}{\Delta t^n}(S^{\alpha,n}_{K,\nu} - S^{\alpha,n-1}_{K,\nu}) - k^\alpha_{m,j_K}(S^{\alpha,n}_{K,\nu,up}) F^\alpha_{K,\nu}(u^{\alpha,n}) \right) \; v^\alpha_\nu \\
\displaystyle + \sum_{\sigma\in\mathcal{F}_\Gamma} \left(\frac{\phi_\sigma}{\Delta t^n}(S_\sigma^{\alpha,n} - S_\sigma^{\alpha,n-1}) + \sum_{\mathbf{s}\in\mathcal{V}_\sigma} k^\alpha_{f,j_\sigma}(S^{\alpha,n}_{\sigma,\mathbf{s},up}) F^\alpha_{\sigma,\mathbf{s}}(u^{\alpha,n}) \right) v^\alpha_\sigma \\
\displaystyle + \sum_{\sigma\in\mathcal{F}_\Gamma} \sum_{\mathbf{s}\in\mathcal{V}_\sigma\setminus\mathcal{V}_{ext}} \left(\frac{\phi_{\sigma,s}}{\Delta t^n}(S^{\alpha,n}_{\sigma,\mathbf{s}} - S^{\alpha,n-1}_{\sigma,\mathbf{s}}) - k^\alpha_{f,j_\sigma}(S^{\alpha,n}_{\sigma,\mathbf{s},up}) F^\alpha_{\sigma,\mathbf{s}}(u^{\alpha,n}) \right) v^\alpha_{\mathbf{s}} = 0.
\end{array}\right. \tag{7}$$

In (7), the phase fluxes are defined by

$$\left\{\begin{array}{rcl}
F^\alpha_{K,\nu}(u) & = & F_{K,\nu}(u) + \rho^\alpha g F_{K,\nu}(Z), \\
F^\alpha_{\sigma,\mathbf{s}}(u) & = & F_{\sigma,\mathbf{s}}(u) + \rho^\alpha g F_{\sigma,\mathbf{s}}(Z),
\end{array}\right. \tag{8}$$

with Z denoting the vector $(z_K, z_{\mathbf{s}}, z_\sigma)_{K\in\mathcal{M},\mathbf{s}\in\mathcal{V},\sigma\in\mathcal{F}_\Gamma}$. The upstream values of the saturations $S^{\alpha,n}_{K,\nu,up}$ and $S^{\alpha,n}_{\sigma,\mathbf{s},up}$ are defined by

$$\left\{\begin{array}{l}
S^{\alpha,n}_{K,\nu,up} = S^{\alpha,n}_K \text{ if } F^\alpha_{K,\nu}(u^{\alpha,n}) \geq 0, \\
S^{\alpha,n}_{K,\nu,up} = S^{\alpha,n}_{K,\nu} \text{ if } F^\alpha_{K,\nu}(u^{\alpha,n}) < 0,
\end{array}\right.
\qquad
\left\{\begin{array}{l}
S^{\alpha,n}_{\sigma,\mathbf{s},up} = S^{\alpha,n}_\sigma \text{ if } F^\alpha_{\sigma,\mathbf{s}}(u^{\alpha,n}) \geq 0, \\
S^{\alpha,n}_{\sigma,\mathbf{s},up} = S^{\alpha,n}_{\sigma,\mathbf{s}} \text{ if } F^\alpha_{\sigma,\mathbf{s}}(u^{\alpha,n}) < 0.
\end{array}\right. \tag{9}$$

As exhibited in Figure 5, the definition of the saturations at the matrix fracture interfaces takes into account the jump of the saturations induced by the different rocktypes. More precisely, for all $K \in \mathcal{M}$ and $\nu \in \Xi_K \setminus \mathcal{V}_{ext}$ we set

$$\begin{array}{ll}
S^{g,n}_K = S^g_{m,j_K}(u^{g,n}_K - u^{w,n}_K), & S^{w,n}_K = 1 - S^{g,n}_K, \\
S^{g,n}_{K,\nu} = S^g_{m,j_K}(u^{g,n}_\nu - u^{w,n}_\nu), & S^{w,n}_{K,\nu} = 1 - S^{g,n}_{K,\nu},
\end{array} \tag{10}$$

and for all $\sigma \in \mathcal{F}_\Gamma$ and $\mathbf{s} \in \mathcal{V}_\sigma \setminus \mathcal{V}_{ext}$ we set

$$\begin{array}{ll}
S^{g,n}_\sigma = S^g_{f,j_\sigma}(u^{g,n}_\sigma - u^{w,n}_\sigma), & S^{w,n}_\sigma = 1 - S^{g,n}_\sigma, \\
S^{g,n}_{\sigma,\mathbf{s}} = S^g_{f,j_\sigma}(u^{g,n}_{\mathbf{s}} - u^{w,n}_{\mathbf{s}}), & S^{w,n}_{\sigma,\mathbf{s}} = 1 - S^{g,n}_{\sigma,\mathbf{s}}.
\end{array} \tag{11}$$

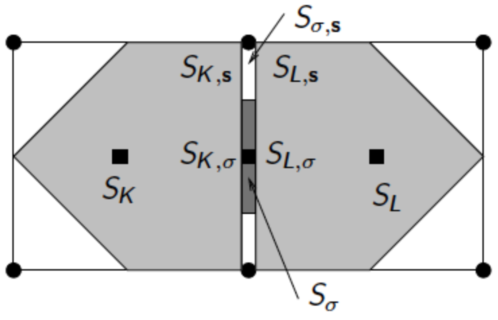

Figure 5: Saturations inside the cells K and L, the fracture face σ and at the matrix fracture interfaces taking into account the saturation jumps induced by the different rocktypes.

3 Solving the System of Nonlinear Equations

Now let us demonstrate how the discretization (7)-(11) can be extended to the case of the inverse capillary pressure graphs satisfying (A_2) but not (A_{2a}).

Let $J = J_m \cup J_f$, for all $K \in \mathcal{M}$ we set $\chi_K = \{j_K\} \in 2^J$. For all $\sigma \in \mathcal{F}_\Gamma$ we set $\chi_\sigma = \{j_\sigma\} \cup \bigcup_{K \,|\, \sigma \in \mathcal{F}_K} \{j_K\}$. For all $\mathbf{s} \in \mathcal{V}$ we set $\chi_{\mathcal{V}} = \bigcup_{K \,|\, \mathbf{s} \in \mathcal{V}_K} \{j_K\} \cup \bigcup_{\sigma \,|\, \mathbf{s} \in \mathcal{V}_\sigma} \{j_\sigma\}$. Then, we define

$$\chi_{\mathcal{D}} = \bigcup_{K \in \mathcal{M}} \chi_K \bigcup_{\sigma \in \mathcal{F}_\Gamma} \chi_\sigma \bigcup_{\mathbf{s} \in \mathcal{V}} \chi_{\mathbf{s}}.$$

The following proposition justifies the fact that a pair of unknowns is sufficient at any degrees of freedom located on the rocktype intersection.

Proposition 3.1 *Let $\chi \in \chi_{\mathcal{D}}$ and $\left(S^g_j\right)_{j \in \chi}$ be a finite family of maximal monotone graphs with domain $\mathbf{R}$ and such that $S^g_j(p) \subset [0,1]$ for all $p \in \mathbf{R}$ and $j \in \chi$. Then there exist a family of continuous piecewise differentiable functions $\mathcal{P}_\chi$ and $\left(\mathcal{S}^g_{\chi,j}\right)_{j \in \chi}$ defined on an open convex set $\mathcal{I} \subset \mathbf{R}$ such that $\mathcal{P}_\chi(\mathcal{I}) = \mathbf{R}$ and such that for $\tau \in \mathcal{I}$ and $j \in \chi$*

$$\mathcal{S}^g_{\chi,j}(\tau) \in S^g_j(\mathcal{P}_\chi(\tau)); \tag{12}$$

moreover they can be chosen such that the following non-degeneracy condition

$$\sum_{j \in \chi} \frac{\mathrm{d}}{\mathrm{d}\tau} \left(\mathcal{S}^g_{\chi,j}(\tau), \mathcal{P}_\chi(\tau)\right) \neq (0,0) \tag{13}$$

is satisfied for a.e. $\tau \in \mathcal{I}$. In addition, without loss of generality on can assume that ${\mathcal{S}^g_{\chi,j}}'(\tau), \mathcal{P}'_\chi(\tau) \geq 0$ for a.e. $\tau \in \mathcal{I}$.

For all $\chi \in \chi_{\mathcal{D}}$ let $\mathcal{P}_\chi$ and $\left(\mathcal{S}^g_{\chi,j}\right)_{j \in \chi}$ be some family of non decreasing functions associated with the family of graphs $\left(S^g_j\right)_{j \in \chi}$ and satisfying (12) and (13).

The saturations are defined by

$$\left\{\begin{array}{lll} S^{g,n}_K = \mathcal{S}^g_{\chi_K, j_K}(\tau^n_K), & S^{w,n}_K = 1 - S^{g,n}_K & \text{for all } K \in \mathcal{M}, \\ S^{g,n}_\sigma = \mathcal{S}^g_{\chi_\sigma, j_\sigma}(\tau^n_K), & S^{w,n}_\sigma = 1 - S^{g,n}_\sigma & \text{for all } \sigma \in \mathcal{F}_\Gamma, \\ S^{g,n}_{K,\nu} = \mathcal{S}^g_{\chi_\nu, j_K}(\tau^n_\nu), & S^{w,n}_{K,\nu} = 1 - S^{g,n}_{K,\nu} & \text{for all } K \in \mathcal{M}, \nu \in \Xi_K, \\ S^{g,n}_{\sigma,\mathbf{s}} = \mathcal{S}^g_{\chi_{\mathbf{s}}, j_\sigma}(\tau^n_{\mathbf{s}}), & S^{w,n}_{\sigma,\mathbf{s}} = 1 - S^{g,n}_{\sigma,\mathbf{s}} & \text{for all } \sigma \in \mathcal{F}_\Gamma, \mathbf{s} \in \mathcal{V}_\sigma, \end{array}\right. \tag{14}$$

and the water pressures by

$$\left\{\begin{array}{ll} u^{w,n}_K = u^{g,n}_K + \mathcal{P}_{\chi_K}(\tau^n_K) & \text{for all } K \in \mathcal{M}, \\ u^{w,n}_\sigma = u^{g,n}_\sigma + \mathcal{P}_{\chi_\sigma}(\tau^n_\sigma) & \text{for all } \sigma \in \mathcal{F}_\Gamma, \\ u^{w,n}_{\mathbf{s}} = u^{g,n}_{\mathbf{s}} + \mathcal{P}_{\chi_{\mathbf{s}}}(\tau^n_{\mathbf{s}}) & \text{for all } \mathbf{s} \in \mathcal{V}. \end{array}\right. \tag{15}$$

The new scheme consist in finding $u^{g,n}, \tau^{w,n} \in X^0_{\mathcal{D}}$, $n = 1, \cdots, N$, satisfying (7), (8), (9) along with (14)-(15).

4 Implementation and Numerical Experiments

In this section we present numerical experiments which aims to compare the robustness and efficiency of the classical pressure-saturation formulation with more advanced choices of primary unknowns which are implemented using the graph parametrization approach presented above. The pressure-pressure formulation is excluded from the comparison since is has a very poor efficiency when dealing with dry (s^g close to 1) media. In practice, the pressure-pressure formulation has also been tested and it failed to converge for matrix fracture capillarity ratio $\frac{b_m}{b_f}$ larger than 10 (see below for the definition of this ratio).

The family of test cases presented here simulates the liquid gas two phase Darcy flow in a tight gas reservoir. The data set is similar to Example 2 of [17] except for the choice of the capillary pressure curves. The reservoir is defined by the domain $\Omega = (-500, 500) \times (-250, 250) \times (-100, 100)$ (in meters). Three transverse fractures $\Gamma_i, i = 1,2,3$ of width $d_f = 0.02$ m are initiated by hydraulic fracturing from a horizontal well. They are defined by the squares $\{x_i\} \times (-50, 50) \times (-50 \times 50)$ with $x_1 = -250$, $x_2 = 0$, $x_3 = +250$. An horizontal well of radius $r_w = 0.1$ m is located along $y = z = 0$ and perforates each fracture $\Gamma_i, i = 1,2,3$ in a triangular equilateral face of center $x_i, y = z = 0$ and of edge size $1m$. During the water injection phase, the water penetrates only a few tens of centimeters in the matrix due to the low permeability of the reservoir. Therefore in order to obtain an accurate water saturation in the neighbourhood of the fractures with a reasonnable number of cells, a strong anisotropic refinement is needed in the normal direction of the fractures in the neihbourhood of each fracture. As exhibited in Figures 6 and 7 this anisotropic refinement is obtained using prismatic meshes with triangular base. In order to match the boundaries of these refined boxes with the surrounding tetrahedral mesh of the reservoir, a layer of pyramids is added arround each fracture box as exhibited in Figures 6. The tetrahedral mesh matching the triangulation of the fracture box boundaries has been obtained using TetGen [18]. Table 1 summarizes the characteristics of the resulting hybrid mesh that will be used in the following numerical test cases.

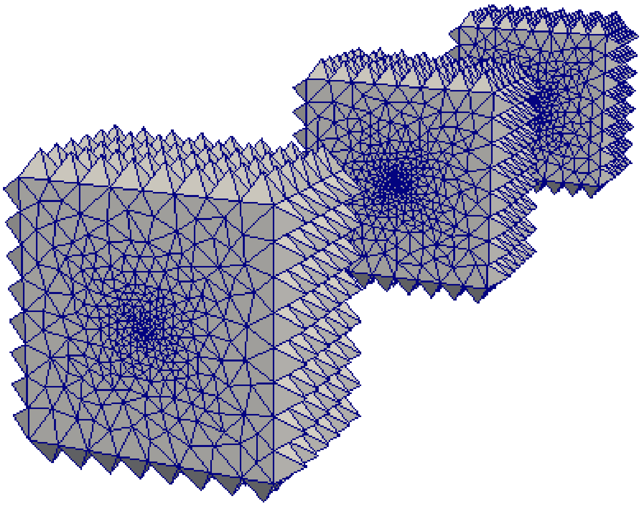

Figure 6: The prismatic meshes with their layer of pyramids for each refined box around each fracture located at the center of each box.

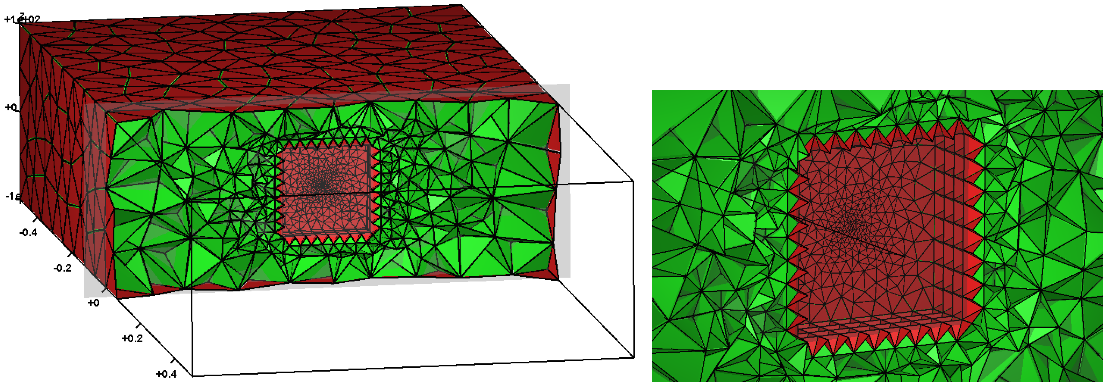

Figure 7: Connection of the prismatic mesh around one fracture with the surrounding tetrahedral mesh using a layer of pyramids.

$\mathbf{N_{cells}}$	$\mathbf{N_{nodes}}$	$\mathbf{N_{FracF}}$	Linear system d.o.f.
232 920	45 193	1 634	46 827

Table 1: Number N_{cells} of cells, number N_{nodes} of nodes, number N_{FracF} of fracture faces and number of unknown in the linear system after the elimination of the cell unknowns (2 unknowns per d.o.f).

We consider only two rocktypes in this test case, the matrix rocktype denoted by $j = m$ and the fracture rocktype denoted by $j = f$. The mobilities are defined for $j = m, f$ by the following Corey law

$$k_j^\alpha(s^\alpha, \mathbf{x}) = \frac{k^\alpha_{j,max}(\bar{s}^\alpha)^{n_j^\alpha}}{\mu^\alpha}, \tag{16}$$

where $\bar{s}^w = \frac{s^w - s^w_{r,j}}{1 - s^w_{r,j} - s^g_{r,j}}$, and $\bar{s}^g = \frac{s^g - s^g_{r,j}}{1 - s^g_{r,j} - s^w_{r,j}}$ are the reduced saturations such that $s^w_{r,m} = 0.2$, $s^w_{r,f} = s^g_{r,m} = s^g_{r,f} = 0$. In the following numerical experiments we have set $k^w_{m,max} = 0.3$, $k^g_{m,max} = 0.6$, $n^w_m = 1.5$, $n^g_m = 3$ in the matrix, and $k^w_{f,max} = k^g_{f,max} = 1$, $n^w_f = n^g_f = 1$ in the fractures.

The capillary pressure/saturation relation are also given for the matrix ($j = m$) and fracture ($j = f$) rocktypes by the following Corey law

$$S^g_j(p) = \begin{cases} 0 & \text{if } \ p - p_{ent,j} < 0, \\ 1 - e^{-\frac{p - p_{ent,j}}{b_j}} & \text{if } \ p - p_{ent,j} \geq 0, \end{cases} \tag{17}$$

where the parameter $p_{ent,j} > 0$ stands for the entry pressure. Both b_j and $p_{ent,j}$ depends on the rocktype $j = m, f$. Figure 8 exhibits, the typical shape of the matrix and fracture capillary pressure graphs P_{cm} and P_{cf}, which are the multi-valued inverses of S^g_m and S^g_f respectively. Remark that, when b_j tends to 0, the graph of S^g_j tends to the graph of the multi-valued Heaviside function centered at $p = p_{ent,j}$. The following numerical experiments will assess the efficiency of the different choices of primary unknowns for different values of the parameters b_j and $p_{ent,j}$, $j = m, f$.

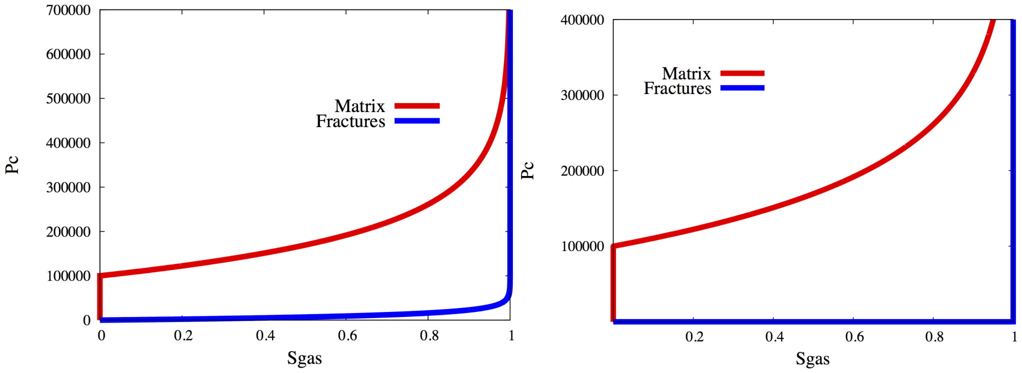

Figure 8: The graphs of the capillary pressures P_{cm} in the matrix, and P_{cf} in the fractures for $b_m = 10^5$ Pa, $b_f = 10^4$ Pa, $p_{ent,m} = 10^5$ Pa, $p_{ent,f} = 0$ (left) and $b_m = 10^5$ Pa, $b_f = 0$, $p_{ent,m} = 10^5$ Pa, $p_{ent,f} = 0$ (right).

The viscosities of the two phases are set to $\mu^w = 10^{-3}$ $\mu^g = 2.35\ 10^{-5}$ Pa·s, and their densities are fixed to the constant value $\rho^w = 1000$ Kg/m^3 for the water phase, and to the perfect gas density $\rho^g(u^g) = \frac{M}{RT}u^g$ Kg/m^3 for the gas phase with $M = 0.016$ Kg corresponding to methane, $R = 8.32$ J·mol^{-1} ·K^{-1}, and $T = 300$ K. The reservoir is initially at the liquid pressure $u^w = 400\ 10^5$ Pa, at the residual water saturation in the matrix and at water saturation close to 0 in the fractures obtained by the continuity of the capillary pressure at the matrix fracture interface. The permeability of the matrix is isotropic and set to $\Lambda_m = \lambda_m \mathrm{Id}$ with $\lambda_m = 2\ 10^{-17}$ m^2, very low compared with the permeability of the fractures $\Lambda_f = \lambda_f \mathrm{Id}$ with $\lambda_f = 2\ 10^{-12}$ m^2. The porosity is equal to $\phi_m = 0.1$ in the matrix and to $\phi_f = 0.3$ in the fractures.

The liquid is first injected at high hydraulic fracturing pressure 1000 10^5 Pa fixed at each perforation during 1 day. Then, the perforations are closed during the next 3 days before the production of gas starts and goes on during the next 296 days at the fixed pressure 300 10^5 Pa in each perforation. The simulation runs over a period of 300 days and the nonlinear systems obtained at each time step are solved by a Newton-Raphson method. The time stepping is defined by an initial time step of 0.001 hour and a maximum time step of 0.05 days during the water injection period, of 0.1 days during the well closure, and of 5 days during the production period. If the Newton method does not converge after 35 iterations, the time step is chopped by a factor 2 and recomputed. The time step is increased by a factor 1.2 after each successful time step until it reaches the maximum time step. The stopping criteria on the relative residuals are fixed to 10^{-6} for the GMRes solver preconditioned by ILU0 and to 10^{-5} for the Newton method.

The following numerical experiments compare the pressure saturation formulation using gas pressure and gas saturation as the primary unknowns with some more advanced parametrizations inspired by variable switch techniques. Since only one fracture and one matrix rocktypes are considered, the set $\mathcal{X}_{\mathcal{D}}$ is equal to

$$\mathcal{X}_{\mathcal{D}} = \{\{m\},\{m,f\}\},$$

where $\chi = \{m\}$ corresponds to degrees of freedom located in the matrix only and $\chi = \{m,f\}$ corresponds to degrees of freedom located at the matrix fracture interfaces. In the following numerical experiments, the primary unknowns for $\chi = \{m\}$ are fixed for both formulations to (u^g, s^g_m) since this is an efficient and simple choice for a single rocktype. The choices of parametrization at the matrix fracture interface i.e. for $\chi = \{m,f\}$ will result in functions $\mathcal{S}^g_m(\tau)$, $\mathcal{S}^g_f(\tau)$, $\mathcal{P}(\tau)$, which we define below for several types of capillary pressures curves given by Corey law. We will distinguish the following five cases ordered with increasing complexity:

(C1) $b_m > 0$, $0 < b_f < b_m$, $p_{ent,m} = p_{ent,f} = 0$;

(C2) $b_m > 0$, $b_f = 0$, $p_{ent,m} = p_{ent,f} = 0$;

(C3) $b_m > 0$, $0 < b_f < b_m$, $p_{ent,m} > 0$, $p_{ent,f} = 0$;

(C4) $b_m > 0$, $b_f = 0$, $p_{ent,m} > 0$, $p_{ent,f} = 0$;

(C5) $b_m = 0$, $b_f = 0$, $p_{ent,m} > 0$, $p_{ent,f} = 0$.

The choices of the primary unknowns will be compared in terms numerical behavior of the simulations based on the number of linear and nonlinear iterations and on the CPU time.

4.1 Zero entry pressures both in the matrix and in the fractures

In this first case, the entry pressures are set to $p_{ent,j} = 0$, $j = m, f$ leading to the following Corey laws

$$S^g_j(p) = \begin{cases} 0 & \text{if } p < 0, \\ 1 - e^{-\frac{p}{b_j}} & \text{if } p \geq 0. \end{cases} \tag{18}$$

In the matrix we fix $b_m = 10^5$ Pa, and we consider a family of values $b_f = 1, 10, 10^2, 10^3, 10^4$ Pa in the fractures. Figure 9 exhibits, for the ratio $\frac{b_m}{b_f} = 10$, the capillary pressure graphs P_{cm} and P_{cf}. For this test cases, the pressure-saturation formulation is compared to the variable switch $(u^g, s^g_f)/(u^g, s^g_m)$ formulation picking the "steepest" saturation unknown, that is to say the one which has a largest derivative with respect to the capillary pressure.

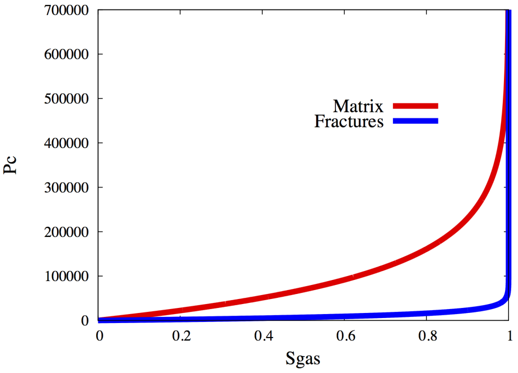

Figure 9: P_{cm} in the matrix and P_{cf} in the fractures.

Pressure-saturation formulation: The formulation is defined by the following set of functions

$$\begin{cases} \mathcal{S}^g_m(\tau) = \tau \\ \mathcal{S}^g_f(\tau) = P_{cf}^{-1}(P_{cm}(\tau)) = 1 - (1-\tau)^{\frac{b_m}{b_f}} \\ \mathcal{P}(\tau) = P_{cm}(\tau) = -b_m \ln(1-\tau) \end{cases} \tag{19}$$

with $\tau \in [0,1)$.

When $\frac{b_m}{b_f}$ goes to infinity (i.e. when the capillary pressure in the fracture network goes to zero), the function $\mathcal{S}_f^g(\tau)$ tends to the graph, which is multi-valued at $\tau = 0$. Numerically, this would lead to the lost of robustness for large values $\frac{b_m}{b_f}$.

Variable-switch formulation: this formulation is obtained using the conditions (12) in the framework of Proposition 3.1 to which we add the following conditions

$$\max\left(\frac{\mathrm{d}\mathcal{S}_m^g}{\mathrm{d}\tau}, \frac{\mathrm{d}\mathcal{S}_f^g}{\mathrm{d}\tau}\right) = 1$$

and

$$\mathcal{S}_m^g(0) = \mathcal{S}_f^g(0) = 0.$$

The computations give (see Figure 10):

$$\mathcal{S}_f^g(\tau) = \begin{cases} \tau, & \tau \in [0,\tau_1), \\ P_{cf}^{-1}(P_{cm}(\tau - \tau_1 + P_{cm}^{-1}(P_{cf}(\tau_1)))) = 1 - (\tau_1 + (1-\tau_1)^{\frac{b_m}{b_f}} - \tau)^{\frac{b_f}{b_m}}, & \tau \in [\tau_1, \tau_2], \end{cases} \tag{20}$$

$$\mathcal{S}_m^g(\tau) = \begin{cases} P_{cm}^{-1}(P_{cf}(\tau)) = 1 - (1-\tau)^{\frac{b_f}{b_m}}, & \tau \in [0,\tau_1), \\ \tau - \tau_1 + P_{cm}^{-1}(P_{cf}(\tau_1)) = \tau - \tau_1 + 1 - (1-\tau_1)^{\frac{b_f}{b_m}}, & \tau \in [\tau_1, \tau_2], \end{cases} \tag{21}$$

$$\mathcal{P}(\tau) = \begin{cases} P_{cf}(\mathcal{S}_f^g(\tau)) = -b_f \ln(1-\tau), & \tau \in [0,\tau_1), \\ P_{cm}(\mathcal{S}_m^g(\tau)) = -b_m \ln(\tau_1 + (1-\tau_1)^{\frac{b_f}{b_m}} - \tau), & \tau \in [\tau_1, \tau_2], \end{cases} \tag{22}$$

where $\tau_1 = 1 - (\frac{b_f}{b_m})^{\frac{b_m}{b_m - b_f}}$ and $\tau_2 = 1 + (1-\tau_1)^{\frac{b_f}{b_m}}$. It is worth to notice that by construction, the derivatives of the functions $\mathcal{S}_f^g(\tau)$, $\mathcal{S}_m^g(\tau)$ and $\mathcal{P}(\tau)$ are continuous at $\tau = \tau_1$.

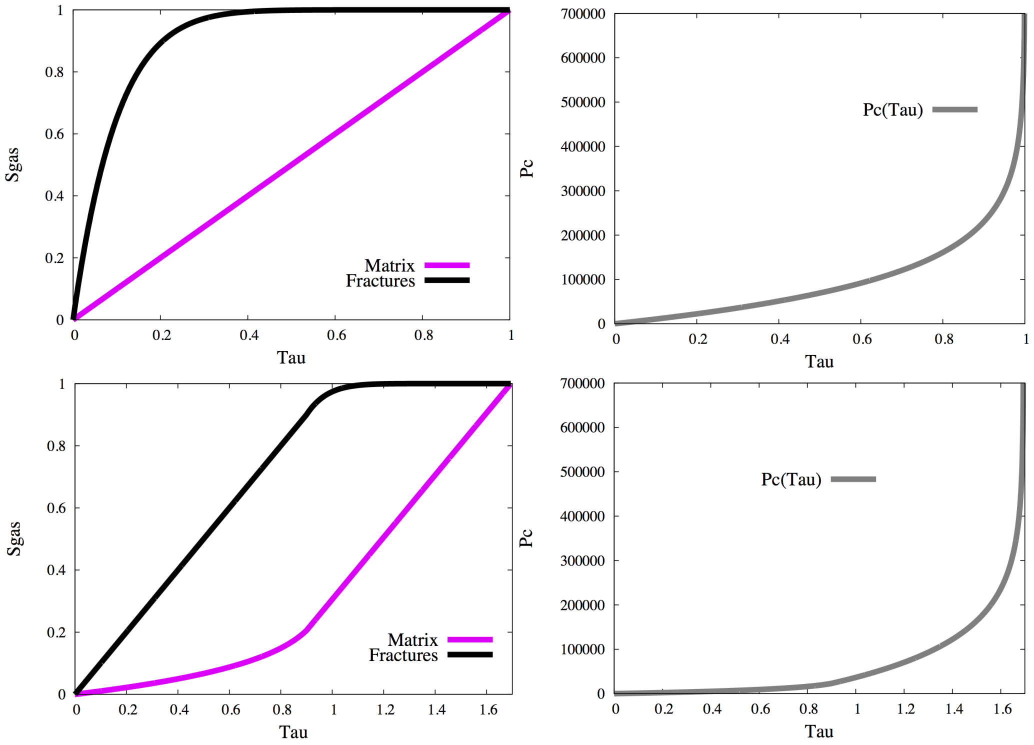

Figure 10: $\mathcal{S}_m^g(\tau)$, $\mathcal{S}_f^g(\tau)$, and $\mathcal{P}(\tau)$ curves for the pressure-saturation formulation (on the top) and for variable switch formulation (at the bottom), obtained for $b_m = 10^5$ Pa, $b_f = 10^4$ Pa, and $p_{ent,m} = p_{ent,f} = 0$.

When, for a fixed b_m, the ratio $\frac{b_m}{b_f}$ goes to infinity, the variable switch parametrization tends to the following formulation (see Figure 11):

$$\mathcal{S}^g_f(\tau) = \begin{cases} \tau, & \tau \in [0, \tau_1), \\ 1, & \tau \in [\tau_1, \tau_2], \end{cases} \tag{23}$$

$$\mathcal{S}^g_m(\tau) = \begin{cases} 0, & \tau \in [0, \tau_1), \\ \tau - \tau_1, & \tau \in [\tau_1, \tau_2], \end{cases} \tag{24}$$

$$\mathcal{P}(\tau) = \begin{cases} 0, & \tau \in [0, \tau_1), \\ (P_{cm}(\mathcal{S}^g_m(\tau)) = -b_m \ln(1 - (\tau - \tau_1)), & \tau \in [\tau_1, \tau_2], \end{cases} \tag{25}$$

with $\tau_1 = 1$, $\tau_2 = 2$. Note that this limit case of a vanishing capillary pressure in the fractures cannot be accounted for by the pressure-saturation formulation.

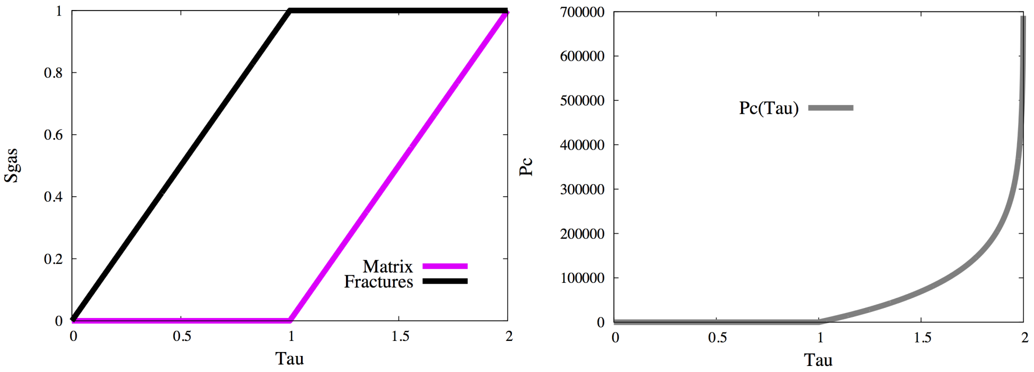

Figure 11: $\mathcal{S}^g_m(\tau)$, $\mathcal{S}^g_f(\tau)$, and $\mathcal{P}(\tau)$ curves for the variable switch formulation obtained for $b_m = 10^5$ Pa, $b_f = 0$, and $p_{ent,m} = p_{ent,f} = 0$.

The numerical behavior of the scheme for both formulations is exhibited in Table 2 showing, for different values of the ratio $\frac{b_m}{b_f}$, the number of successful time steps, the number of time step chops, the number of Newton iterations by successful time steps, the number of GMRes iterations by Newton iteration, and the CPU time. The variable switch formulation turns out to be more efficient and more robust w.r.t. the value of $\frac{b_m}{b_f}$ both in terms of number of Newton iterations and the number of time step chops. Note that, as it can be expected, for $\frac{b_m}{b_f} = \infty$ the variable switch formulation performs similarly that for the case $\frac{b_m}{b_f} = 10^5$.

	pressure-saturation					**variable switch**				
$\frac{b_m}{b_f}$	**N$_{\text{dt}}$**	**N$_{\text{Chop}}$**	**N$_{\text{Newton}}$**	**N$_{\text{GMRes}}$**	**CPU(s)**	**N$_{\text{dt}}$**	**N$_{\text{Chop}}$**	**N$_{\text{Newton}}$**	**N$_{\text{GMRes}}$**	**CPU(s)**
10	226	2	4.2	25.9	4 638	226	2	4.3	26.2	5 523
10^2	294	21	10.7	20.1	14 557	246	8	7.5	22.2	9 016
10^3	297	22	11.7	19.7	16 183	225	1	5.5	24.2	6 245
10^4	304	24	12.9	19.8	17 742	225	1	4.8	25.1	5 492
10^5	313	26	12.8	19.6	18 346	235	4	5.4	23.9	6 260
∞	n/a	n/a	n/a	n/a	n/a	235	4	5.3	23.9	6 448

Table 2: Numerical results for the pressure-saturation and variable switch formulations for $b_m = 10^5$ Pa, $p_{ent,m} = p_{ent,f} = 0$, and different values of the ratio $\frac{b_m}{b_f}$: number N_{dt} of successful time steps, number N_{Chop} of time step chops, number N_{Newton} of Newton iterations per successful time step, number N_{GMRes} of GMRes iterations by Newton iteration, and CPU time in seconds.

4.2 Nonzero Entry Pressure in the matrix

Next we consider the test cases with non zero entry pressure in the matrix setting $p_{ent,m} = 10^5$ Pa and $p_{ent,f} = 0$. The graphs of P_{cj}, $j = m, f$ are represented in Figure 8.

Pressure-saturation formulation: At the matrix fracture interface the capillary pressure (see Figure 8) can not be expressed as a function of s_m^g for $p < p_{ent,m}$, but it is however a function of s_f^g. At the matrix fracture interfaces we choose s_f^g as primary unknown, which leads to

$$\mathcal{S}_f^g(\tau) = \tau, \qquad \mathcal{P}_m(\tau) = (S_f^g)^{-1}(\tau) = -b_f \ln(1-\tau),$$

and

$$\mathcal{S}_m^g(\tau) = \begin{cases} 0, & \tau < S_f^g(p_{ent,m}) = 1 - e^{\frac{-p_{ent,m}}{b_f}}, \\ P_{cm}^{-1}(P_{cf}(\tau)) = 1 - e^{\frac{p_{ent,m}}{b_m}}(1-\tau)^{\frac{b_f}{b_m}}, & \tau \geq 1 - e^{\frac{-p_{ent,m}}{b_f}}. \end{cases}$$

Remark that when $\frac{b_m}{b_f}$ goes to infinity the function $P_{cm}^{-1}(P_{cf}(\tau))$ becomes multi-valued at $\tau = 1$ which results in severe numerical instabilities. As a result, we were unable to obtain the convergence of the nonlinear solver for $\frac{b_m}{b_f} > 10$.

Variable-switch formulation: When $b_f = 0$ it is clear that the capillary pressure is no longer a function of the saturation for its values in the interval $(0, p_{ent,m})$. Actually, for those values of capillary pressure the relevant pair of unknowns is (u^w, u^g). This leads to the following formulation, which roughly speaking switches between the three unknowns s_f^g, P_c, and s_m^g

$$\mathcal{S}_f^g(\tau) = \begin{cases} \tau, & \tau \in [0, \tau_1), \\ P_{cf}^{-1}(p_{ent,m}(\tau-\tau_1) + P_{cf}(\tau_1)) = 1 - (1-\tau_1)e^{-\frac{p_{ent,m}}{b_f}(\tau-\tau_1)}, & \tau \in [\tau_1, \tau_2), \\ P_{cf}^{-1}(P_{cm}(\tau-\tau_2)) = 1 - (1-(\tau-\tau_2))^{\frac{b_m}{b_f}} e^{\frac{-p_{ent,m}}{b_f}}, & \tau \in [\tau_2, \tau_3], \end{cases} \tag{26}$$

$$\mathcal{S}_m^g(\tau) = \begin{cases} 0, & \tau \in [0, \tau_2), \\ \tau - \tau_2, & \tau \in [\tau_2, \tau_3], \end{cases} \tag{27}$$

$$\mathcal{P}(\tau) = \begin{cases} P_{cf}(\tau) = -b_f \ln(1-\tau), & \tau \in [0, \tau_1), \\ p_{ent,m}(\tau-\tau_1) + P_{cf}(\tau_1) = p_{ent,m}(\tau-\tau_1) - b_f \ln(1-\tau_1), & \tau \in [\tau_1, \tau_2), \\ P_{cm}(\tau-\tau_2) = p_{ent,m} - b_m \ln(1-(\tau-\tau_2)), & \tau \in [\tau_2, \tau_3]. \end{cases} \tag{28}$$

One can see that $P_{cf}(\tau_1) < p_{ent,m}$ and the derivatives of the functions $\mathcal{S}_f^g(\tau)$, $\mathcal{S}_m^g(\tau)$, $\mathcal{P}(\tau)$ are continuous at $\tau = \tau_1$, where $\tau_1 = 1 - \frac{b_f}{p_{ent,m}}$. Also we define $\tau_2 = \tau_1 + 1 - \frac{P_{cf}(\tau_1)}{p_{ent,m}}$ and $\tau_3 = \tau_2 + 1$ such that $\mathcal{P}(\tau_2) = p_{ent,m}$ and $\mathcal{S}_m^g(\tau_3) = 1$. When the ratio $\frac{b_m}{b_f}$ goes to infinity (see Figure 13) the following formulas are recovered

$$\mathcal{S}_f^g(\tau) = \begin{cases} \tau, & \tau \in [0, \tau_1), \\ 1, & \tau \in [\tau_1, \tau_3], \end{cases} \tag{29}$$

$$\mathcal{S}_m^g(\tau) = \begin{cases} 0, & \tau \in [0, \tau_2), \\ \tau - \tau_2, & \tau \in [\tau_2, \tau_3], \end{cases} \tag{30}$$

$$\mathcal{P}(\tau) = \begin{cases} 0, & \tau \in [0, \tau_1), \\ p_{ent,m}(\tau-\tau_1), & \tau \in [\tau_1, \tau_2), \\ P_{cm}(\mathcal{S}_m^g(\tau) = -b_m \ln(1-(\tau-\tau_2)) + p_{ent,m}, & \tau \in [\tau_2, \tau_3], \end{cases} \tag{31}$$

where $\tau_1 = 1$, $\tau_2 = 2$, and $\tau_3 = 3$.

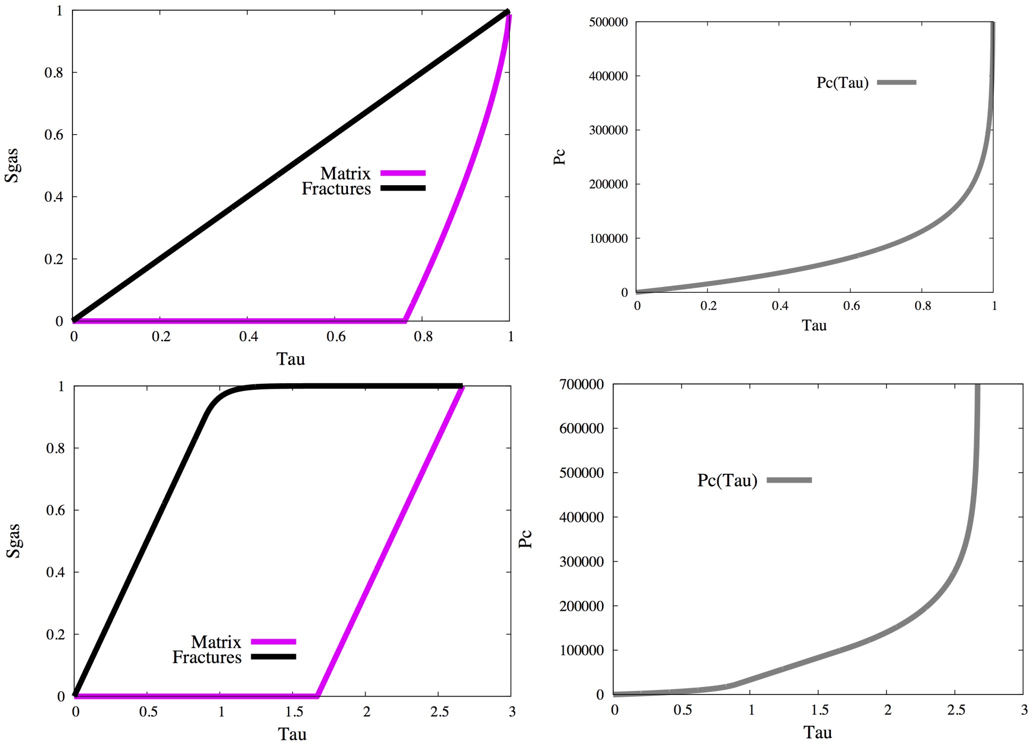

Figure 12: $\mathcal{S}_m^g(\tau)$, $\mathcal{S}_f^g(\tau)$, and $\mathcal{P}(\tau)$ curves for the pressure-saturation formulation (on the top) and variable switch formulation (at the bottom) for $b_m = 10^5$ Pa, $b_f = 10^4$ Pa, $p_{ent,m} = 10^5$ Pa, $p_{ent,f} = 0$.

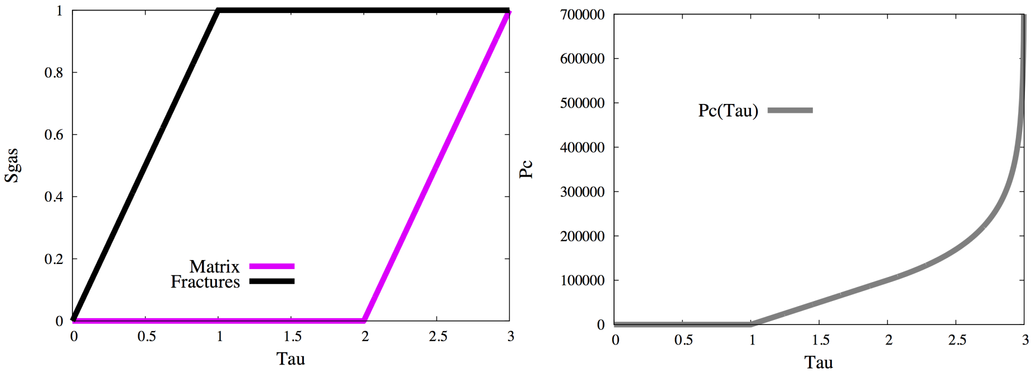

Figure 13: $\mathcal{S}_m^g(\tau)$, $\mathcal{S}_f^g(\tau)$, and $\mathcal{P}(\tau)$ curves for variable switch formulation for $b_m = 10^5$ Pa, $b_f = 0$, $p_{ent,m} = 10^5$ Pa, $p_{ent,f} = 0$.

	pressure-saturation					**variable switch**				
$\frac{b_m}{b_f}$	$\mathbf{N_{dt}}$	$\mathbf{N_{Chop}}$	$\mathbf{N_{Newton}}$	$\mathbf{N_{GMRes}}$	**CPU(s)**	$\mathbf{N_{dt}}$	$\mathbf{N_{Chop}}$	$\mathbf{N_{Newton}}$	$\mathbf{N_{GMRes}}$	**CPU(s)**
2	221	0	3	29.2	3 937	221	0	3.1	28.9	4 479
10	398	52	9.9	20.2	23 400	262	13	6.8	22.7	10 378
10^2	n/c	n/c	n/c	n/c	n/c	269	14	9.9	20.8	14 185
10^3	n/c	n/c	n/c	n/c	n/c	285	18	8.9	20.1	13 740
10^4	n/c	n/c	n/c	n/c	n/c	242	6	6.9	22.8	9 067
10^5	n/c	n/c	n/c	n/c	n/c	276	16	7.5	21.3	11 516
∞	n/a	n/a	n/a	n/a	n/a	299	22	8.1	19.1	10 770

Table 3: Numerical results for the pressure-saturation and variable switch formulations for $b_m = 10^5$ Pa, $p_{ent,m} = 10^5$ Pa, $p_{ent,f} = 0$ and different values of the ratio $\frac{b_m}{b_f}$: number N_{dt} of successful time steps, number N_{Chop} of time step chops, number N_{Newton} of Newton iterations per successful time step, number N_{GMRes} of GMRes iterations by Newton iteration, and CPU time in seconds.

As in the previous case the variable switch formulation is robust w.r.t. the value of $\frac{b_m}{b_f}$ both in terms of number of Newton iterations and the number of time step chops (see Table 3), and allows to deal with full range of the ratio $\frac{b_m}{b_f}$. On the other hand, the pressure-saturation formulation fails to converge except for very small ratios.

4.3 Nonzero Entry Pressure Curves - Other Extensions

We conclude by the case $b_m = b_f = 0$, $p_{ent,m} = 10^5$ Pa, and $p_{ent,f} = 0$ (see Figure 14). This test case can only be treated using the formulation involving multiple primary variable switches.

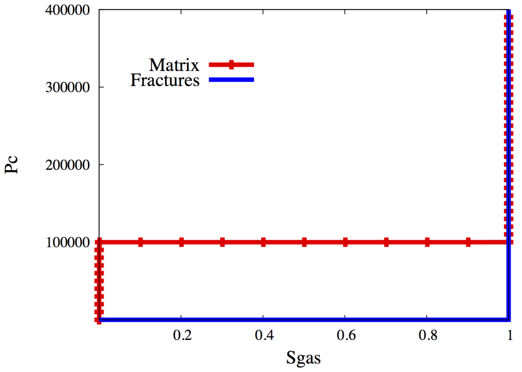

Figure 14: The capillary pressure curves P_{cm} in the matrix and P_{cf} in the fractures for $b_m = b_f = 0$, $p_{ent,m} = 10^5$ Pa, and $p_{ent,f} = 0$.

In the spirit of the previous case we define the following parametrization:

$$\mathcal{S}^g_f(\tau) = \left\{ \begin{array}{ll} \tau, & \tau \in [0, \tau_1), \\ 1, & \tau \in [\tau_1, \tau_3), \end{array} \right. \tag{32}$$

$$\mathcal{S}^g_m(\tau) = \left\{ \begin{array}{ll} 0, & \tau \in [0, \tau_2), \\ \tau - \tau_2, & \tau \in [\tau_2, \tau_3], \end{array} \right. \tag{33}$$

$$\mathcal{P}(\tau) = \left\{ \begin{array}{ll} 0, & \tau \in [0, \tau_1), \\ p_{ent,m}(\tau - \tau_1), & \tau \in [\tau_1, \tau_2), \\ p_{ent,m}, & \tau \in [\tau_2, \tau_3], \end{array} \right. \tag{34}$$

with $\tau_1 = 1$, $\tau_2 = 2$, and $\tau_3 = 3$.

The curves $\mathcal{S}^g_m$, $\mathcal{S}^g_f$ and $\mathcal{P}$ are exhibited in Figure 15. Table 4 shows the good performance of the proposed formulation in terms of time step chops and Newton iterations which confirms the efficiency of the proposed method. Note that, for this test case, we have adapted the Newton solver such that if the Newton iterate for the τ variable tries to jump from above to below the value $\tau_i = \tau_1, \tau_2$ (or from below to above), it is projected onto $\tau = \tau_i + \epsilon$ ($\tau = \tau_i - \epsilon$ correspondingly).

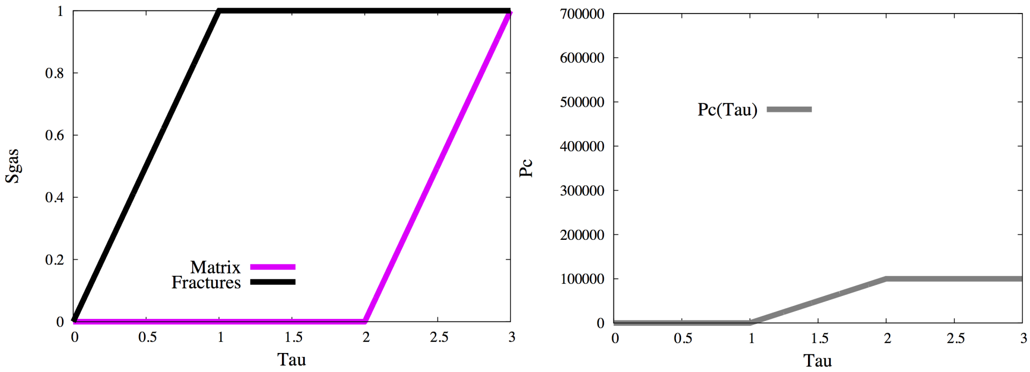

Figure 15: $\mathcal{S}^g_m(\tau)$, $\mathcal{S}^g_f(\tau)$, and $\mathcal{P}(\tau)$ curves for variable switch formulation for $b_m = b_f = 0$, $p_{ent,m} = 10^5$ Pa, and $p_{ent,f} = 0$.

variable switch				
$\mathbf{N_{dt}}$	$\mathbf{N_{Chop}}$	$\mathbf{N_{Newton}}$	$\mathbf{N_{GMRes}}$	**CPU(s)**
221	0	5.8	26.3	5 948

Table 4: Numerical results for the pressure-saturation and variable switch formulations for $b_m = b_f = 0$, $p_{ent,m} = 10^5$ Pa, and $p_{ent,f} = 0$: number N_{dt} of successful time steps, number N_{Chop} of time step chops, number N_{Newton} of Newton iterations per successful time step, number N_{GMRes} of GMRes iterations by Newton iteration, and CPU time in seconds.

4.4 Physical discussion

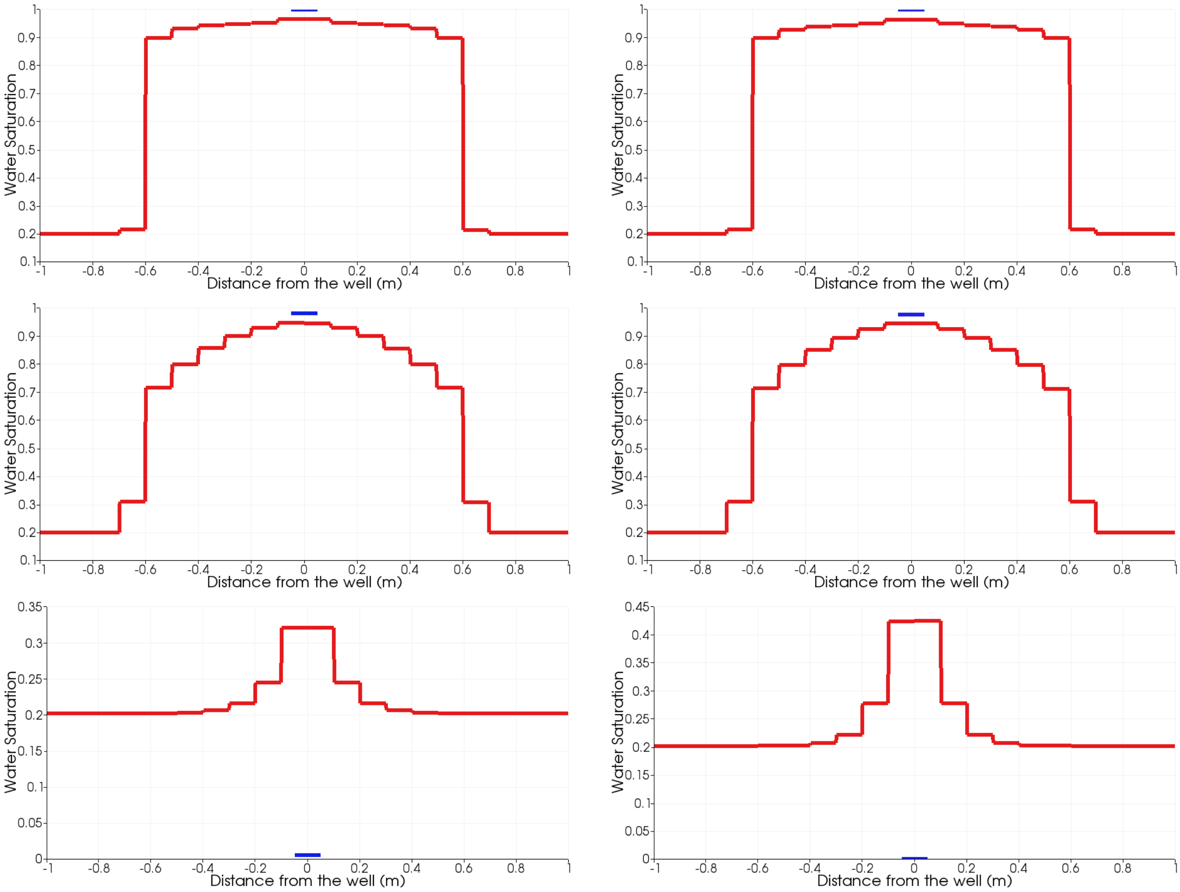

Figure 16: Water saturation in the perforated face in the fracture at $\mathbf{x} = 0$ (blue) and cut of the water saturation in the matrix (red) along the line $y = z = 0$ as a function of the distance to the fracture at the end of each simulation period $t = 1$ day (top), $t = 4$ days (middle) and $t = 300$ days (bottom). The left plots (a) correspond to $b_m = 10^5$ Pa, $b_f = 10^4$ Pa, $p_{ent,m} = p_{ent,f} = 0$, and the right plots (b) to $b_m = 10^5$ Pa, $b_f = 0$, $p_{ent,m} = p_{ent,f} = 0$

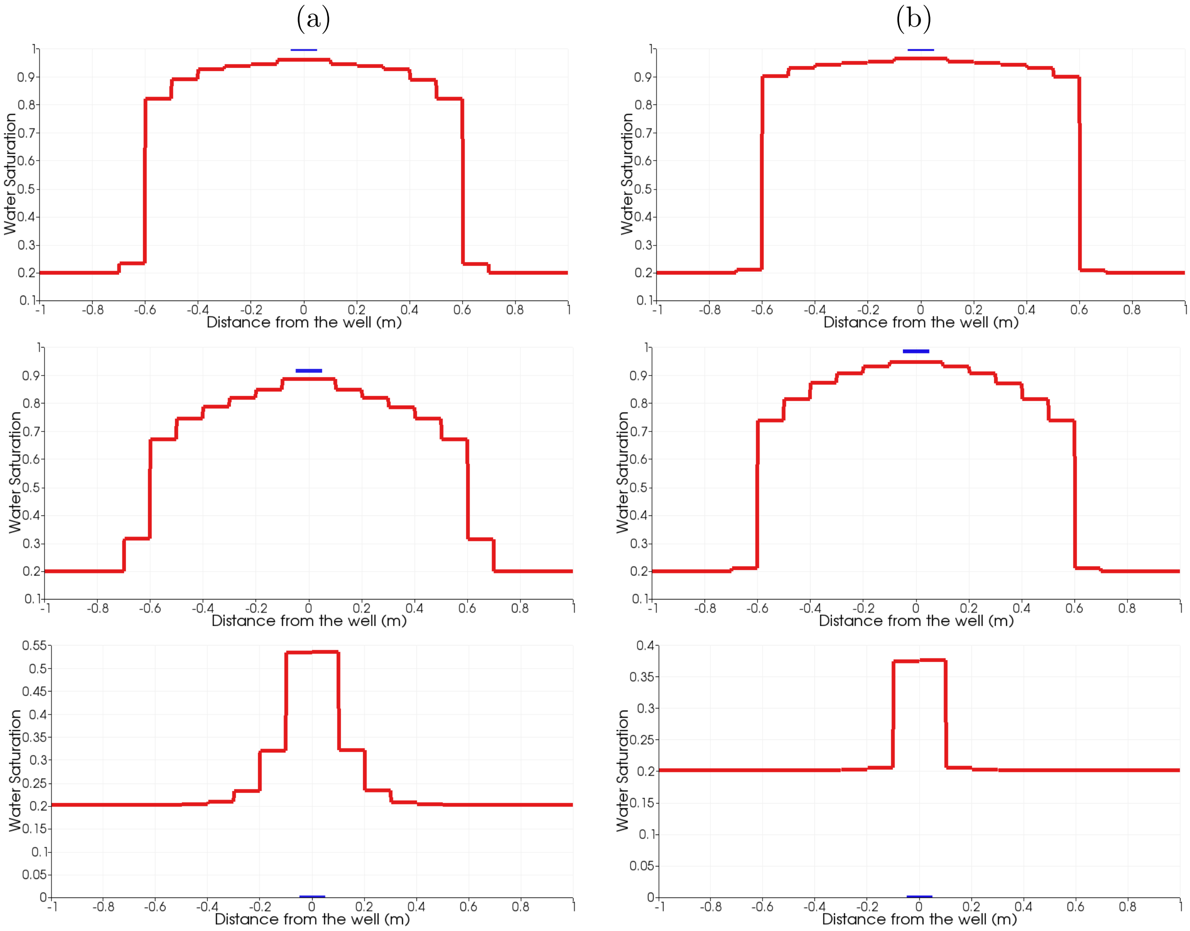

Figure 17: Water saturation in the perforated face in the fracture at $\mathbf{x} = 0$ (blue) and cut of the water saturation in the matrix (red) along the line $y = z = 0$ as a function of the distance to the fracture at the end of each simulation period $t = 1$ day (top), $t = 4$ days (middle) and $t = 300$ days (bottom). The left plots (a) correspond to $b_m = 10^5$ Pa, $b_f = 0$, $p_{ent,m} = 10^5$ Pa, $p_{ent,f} = 0$, and the right plots (b) to $b_m = b_f = 0$, $p_{ent,m} = 10^5$ Pa, $p_{ent,f} = 0$.

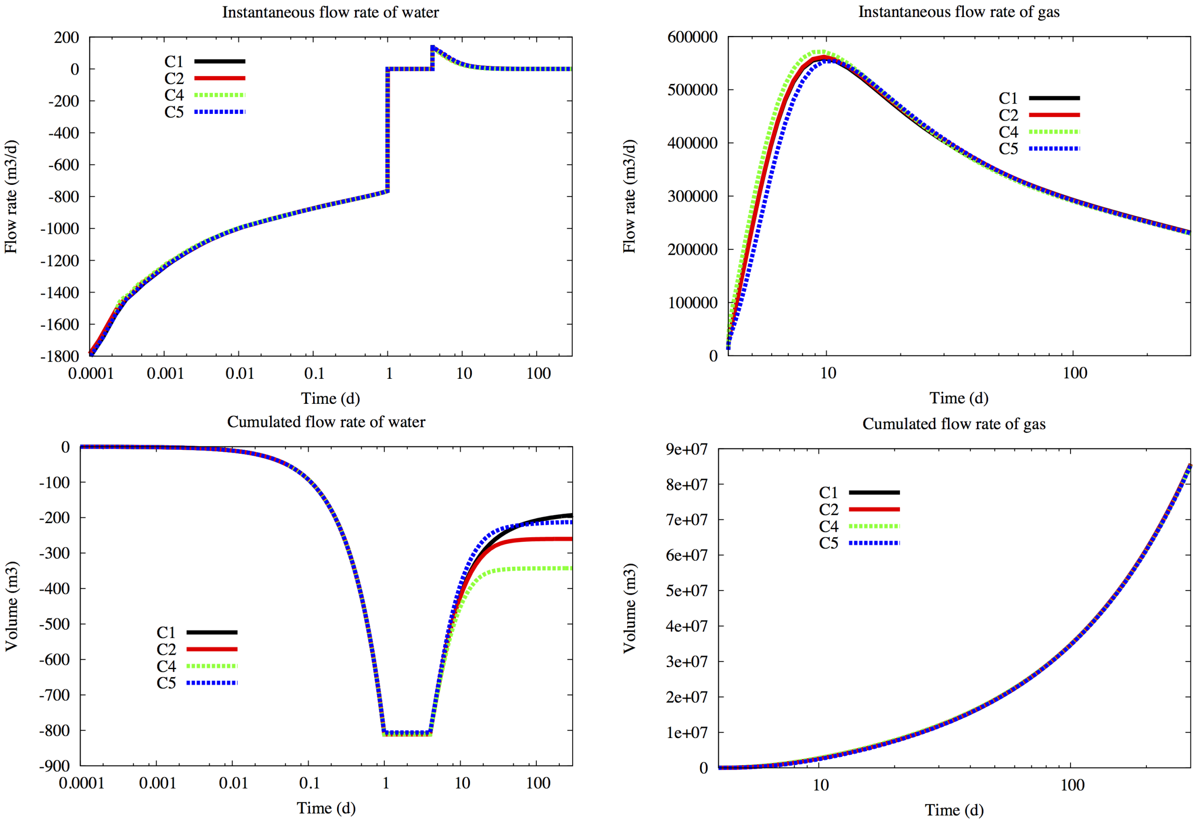

Figure 18: On the top: instantaneous flow rates of water (left) and of gas (right) in $\mathrm{m}^3/\mathrm{day}$ at the bottom: cumulated flow rates of water (left) and gas (right) in m^3 as a function of time, for the following four test cases. CC: $b_m = 10^5$ Pa, $b_f = 10^4$ Pa, $p_{ent,m} = p_{ent,f} = 0$, CF: $b_m = 10^5$ Pa, $b_f = 0$, $p_{ent,m} = p_{ent,f} = 0$, CFPE: $b_m = 10^5$ Pa, $b_f = 0$, $p_{ent,m} = 10^5$ Pa, $p_{ent,f} = 0$, FFPE: $b_m = b_f = 0$, $p_{ent,m} = 10^5$ Pa, $p_{ent,f} = 0$.

Figures 16 and 17 exhibit, at the end of each simulation period at $t = 1$ day, $t = 4$ days and $t = 300$ days, the water saturation in the perforated face in the fracture and the cut of the water saturation in the matrix along the line $y = z = 0$ as a function of the distance to the fracture. One clearly sees that the water phase fills the fractures during the water injection period and penetrates the matrix less than one meter from the fractures. At the end of the well closure period, water has been sucked by imbibition from the fractures to the matrix. At the end of the simulation, the fractures are again fully filled with the gas phase and the water phase above the residual saturation is only partially removed during the production period due to the water retention by capillary effect. Figure 18 exhibits the instantaneous and cumulated flow rates of water and gas at the well with a positive value for production and a negative value for injection. It can be checked in Figures 16, 17 and 18 that the larger the difference between the capillary pressure in the matrix and in the fractures, the more water is retained by the capillary effect into the matrix and at the same time the less water and the more gas are produced.

5 Conclusions

This paper has introduced a general framework for the formulation of two phase Darcy flows with discontinuous capillary pressure curves at rocktype interfaces. This framework is based on the parametrization of the capillary pressure monotone graphs and allow to (1) capture the jumps of the saturations at the different rocktype interfaces, (2) maintain the minimal number of primary unknowns per degree of freedom, (3) deal with arbitrary capillary functions including multi-valued saturation curves. This framework has been tested on a family of tight gas recovery test cases and compared with the classical pressure-saturation formulation using the Vertex Approximate Gradient scheme for gas liquid hybrid dimensional Darcy flows in fractured porous media. The numerical results show clearly the robustness and efficiency of our approach for a wide range of capillary functions with highly constrasted matrix and fracture rocktypes.

6 Acknowledgements

The authors would like to thank GDFSuez EP and Storengy for supporting this work.

References

[1] C. Alboin, J. Jaffre, J. Roberts, and Serres C. Modeling fractures as interfaces for flow and transport in porous media. *Fluid flow and transport in porous media*, 295:13–24, 2002.

[2] K. Brenner, M. Groza, C. Guichard, G. Lebeau, and R. Masson. Gradient discretization of hybrid dimensional darcy flows in fractured porous media. *Numerische Mathematik*, pages 1–41, 2015.

[3] V. Reichenberger, H. Jakobs, P. Bastian, and R. Helmig. A mixed-dimensional finite volume method for multiphase flow in fractured porous media. *Adv. Water Resources*, 29:1020–1036, 2006.

[4] J. Monteagudu and A. Firoozabadi. Control-volume model for simulation of water injection in fractured media: incorporating matrix heterogeneity and reservoir wettability effects. *SPE Journal*, 12:355–366, 2007.

[5] J. Hoteit and A. Firoozabadi. An efficient numerical model for incompressible two-phase flow in fracture media. *Advances in Water Resources*, 31:891–905, 2008.

[6] K. Brenner, M. Groza, C. Guichard, and R. Masson. Vertex approximate gradient scheme for hybrid dimensional two-phase darcy flows in fractured porous media. *Mathematical Modelling and Numerical Analysis*, 49:303–330, 2015.

[7] E. Flauraud, F. Nataf, I. Faille, and R. Masson. Domain decomposition for an asymptotic geological fault modeling. *Comptes Rendus à l'académie des Sciences, Mécanique*, 331:849–855, 2003.

[8] V. Martin, J. Jaffré, and J.E. Roberts. Modeling fractures and barriers as interfaces for flow in porous media. *SIAM J. Sci. Comput.*, 26:1667–1691, 2005.

[9] P. Angot, F. Boyer, and F. Hubert. Asymptotic and numerical modelling of flows in fractured porous media. *Mathematical Modelling and Numerical Analysis*, 43:239–275, 2009.

[10] M. Karimi-Fard, L.J. Durlovski, and K. Aziz. An efficient discrete-fracture model applicable for general-purpose reservoir simulators. *SPE Journal*, 2004.

[11] X. Tunc, I. Faille, T. Gallouët, M.C. Cacas, and P. Havé. A model for conductive faults with non matching grids. *Comp. Geosciences*, 16:277–296, 2012.

[12] T.H. Sandve, I. Berre, and J.M. Nordbotten. An efficient multi-point flux approximation method for discrete fracture-matrix simulations. *Journal of Computational Physics*, 231:3784–3800, 2012.

[13] R. Ahmed, M.G. Edwards, S. Lamine, and B.A.H. Huisman. Control-volume distributed multi-point flux approximation coupled with a lower-dimensional fracture model. *Journal of Computational Physics*, 284:462–489, 2015.

[14] C. Cancès and M. Pierre. An existence result for multidimensional immiscible two-phase flows with discontinuous capillary pressure field. *SIAM J. Math. Anal.*, 44:966–992, 2012.

[15] R. Eymard, C. Guichard, R. Herbin, and R. Masson. Gradient schemes for two-phase flow in heterogeneous porous media and richards equation. *ZAMM - Journal of Applied Mathematics and Mechanics*, 94:560–585, 2014.

[16] R. Eymard, C. Guichard, and R. Herbin. Small-stencil 3d schemes for diffusive flows in porous media. *Mathematical Modelling and Numerical Analysis*, 46:265–290, 2010.

[17] D.Y. Ding, H. Langouet, and L. Jeannin. Simulation of fracturing induced formation damage and gas production from fractured wells in tight gas reservoirs. *SPE*, 153255, 2012.

[18] H. Si. `http://tetgen.org`, 2011.